Proceedings of the ASME 2013 Summer Heat Transfer Conference
HT2013
July 14-19, 2013, Minneapolis, MN, USA

DRAFT HT2013-17302

A FAST COUPLED SOLVER FOR PHONON TRANSPORT IN COMPOSITES

James M. Loy
The University of Texas at Austin
Austin, TX USA

Ajay Vadakkepatt
The University of Texas at Austin
Austin, TX USA

Sanjay R. Mathur
The University of Texas at Austin
Austin, TX USA

Jayathi Y. Murthy
The University of Texas at Austin
Austin, TX USA

ABSTRACT

In recent years, computational techniques for solving phonon transport have been developed under the framework of the semiclassical Boltzmann Transport Equation (BTE). Early work addressed gray transport, but more recent work has begun to resolve wave vector and polarization dependence, including that in relaxation times. Because the relaxation time in typical materials of interest spans several orders of magnitude, typical solution techniques must address an enormous range of Knudsen numbers in the same problem. Calculation procedures which solve the BTE in phase space sequentially work well in the ballistic limit, but are slow to converge in the thick limit. Unfortunately, both extremes may be encountered simultaneously in typical wave-number ***(K)*** -resolved phonon transport problems. In previous work, we developed the coupled ordinate method (COMET) to address this problem. COMET employs a point-coupled solution to resolve coupling in ***K***-space, and embeds this point solver as a relaxation sweep in a geometric multigrid method to maintain spatial coupling. We have demonstrated speedups of up to 200 over conventional sequential solution procedures using this method. COMET also exhibits excellent scaling on multiprocessor platforms, far beyond those obtained by sequential solvers.

In this paper, we extend COMET to address interface transport in composites. Just as scattering couples phonons of different wave vectors in the bulk, reflection and transmission couple different wave vectors together at interfaces. Again, sequential solution procedures perform poorly because of the poor algorithmic coupling in ***K*** space. A computational procedure based on COMET is developed for composites, addressing multigrid agglomeration strategies to promote stronger ***K***-space coupling at interfaces. The technique is applied to canonical superlattice geometries and superior performance over typical sequential solvers is demonstrated. Furthermore, the method is applied to realistic particle composites employing computational meshes developed from x-ray computed tomography (CT) scans of particulate beds. It is demonstrated to yield solutions where sequential solution techniques fail to converge at all.

INTRODUCTION

Thermoelectric devices have been gaining popularity in the research community in recent years [1–8]. The target of much of the research has been finding and creating novel nanostructured materials which have the best figure of merit, $ZT=S^2\sigma T/k$ [9], where S is the Seebeck coefficient, σ the electrical conductivity, and T the operating temperature. Current work has focused on reducing the value of the total thermal conductivity, k, which is made up of an electric contribution and a phononic contribution. For typical semiconducting materials, the electronic contribution to the thermal conductivity is very small and is often neglected. Hence, a lot of work has been directed at reducing the thermal conductivity due to phonon transport.

Since the discovery of thermoelectricity in semiconductors in the 1950s and until recently, it was thought that the best way to reduce the conductivity of phonons was by using atomically heavy materials to slow the group velocity in tandem with alloy scattering to impede short wave length phonons. Particularly, PbTe, SiGe, and $Bi_2Te_3/Sb_2Te_3/Bi_2Se_3$ have been employed in thermoelectric applications [10]. Despite being researched for over 50 years, this class of materials has only been able to achieve a ZT of about 1.2. More recently a further reduction in the lattice conductivity was attained by introducing nanostructures [1,2,5,11–13]. In [11], a room temperature ZT of 2.4 was attained by using a Bi_2Te_3/Sb_2Te_3 superlattice which reduced the phonon thermal

conductivity while not significantly reducing the electrical conductivity. Hsu *et al.* [13] achieved a *ZT* at 800 K of 2.4 using $Ag_nPb_mSb_nTe_{m+2n}$ materials and attributed the increase to the formation of nanodots of Ag and Pb inside a matrix of PbTe. These nanodots acted to scatter phonons and reduce thermal conductivity. Similar to this, in [1,2,5] nanoscructures were created by ball milling bulk materials and then fusing the resulting nanopowder. [1] used nanograins alone to obtain a peak *ZT* of 1.4 for BiSbTe bulk alloys, while [2,5] also used modulation doping to simultaneously increase the carrier mobility to achieve a peak *ZT* of ~1.2 for SiGe nanocomposites. From the above examples, it is clear that phonon scattering at interfaces is a crucial mechanism in reducing the phononic contribution in engineered nanostructured materials. For these reductions to occur, the distance between interfaces must be smaller than the dominant phonon mean free paths in the direction of heat transport. In order to effectively engineer devices which utilize this mechanism, it is necessary to have the ability to simulate the details of phonon transport between and across interfaces.

When the length scales of interest are longer than the phonon wavelength, phase coherence effects are negligible and a particle view point may be adopted. In this limit, the phonon Boltzmann transport equation (BTE) may be employed to compute phonon transport. Solutions to the BTE have been both deterministic and stochastic. The Monte Carlo (MC) method first came about in [14] and has had subsequent improvements [15–17]. This method has also been adapted to include phonon scattering at interfaces [18,19]. Typically, deterministic sequential solution procedures have been the norm in solving the phonon BTE [20–22]. In this procedure, a discrete point in wave vector space is selected and the phonon distribution for that wave vector is solved for in physical space. Then the next discrete point in wave vector space is selected and all of physical space is iteratively solved. This procedure repeats until all wave vector space has been visited, the residual is checked and the decision to continue or stop is made. Though very simple to implement, the convergence of the sequential procedure suffers when the domain is larger than the phonon mean free path. This is because coupling in $\boldsymbol{K}$-space dominates over that in physical space at low Knudsen numbers ($Kn=v\tau/L$). In [23], Loy et al. adapted the coupled ordinates method (COMET) for radiative heat transfer for the solution of the phonon BTE. Excellent acceleration over a wide range of Knudsen number was observed. This success was attributed to the inversion of the solution procedure, whereby a single point in physical space is selected and all of wave vector space is solved directly. The next point in physical space is selected and all of wave vector space is solved. This procedure is embedded in a geometric multigrid to tighten spatial coupling. Thus both physical and $\boldsymbol{K}$-space coupling are addressed efficiently.

The inclusion of interfaces in the solution of the phonon BTE has been introduced in the past using the acoustic mismatch model (AMM) [24], the diffuse mismatch model (DMM) [25], and the atomistic Green's function (AGF) [26]. These interface models couple phonon groups in wave vector space because of transmission and reflection. This coupling is poorly addressed by sequential solution procedures, as discussed above. For fully-resolved nanoparticle composites, which are dominated by interface transport, there is little or no hope of computing converged solutions using sequential methods.

In this paper, we will extend the method developed in [23] to include phonon transport across interfaces with a view to computing phonon transport in realistic composites. The framework inherent in COMET suggests that an interface may be thought of as an operator which projects phonon energy in one $\boldsymbol{K}$ state on to a different set of energy (or $\boldsymbol{K}$) states. This interface operator acts as a general framework which can be tailored to the specific interface model pertinent to the physics of a problem. A comparison with the typical sequential solution procedure is performed for a few simple one-dimensional composites and the performance of the COMET algorithm for interface dominated problems is explored. Finally, COMET is applied to $\boldsymbol{K}$-resolved phonon transport in a real particle composite whose geometry is reconstructed from scanning electron microscopy (SEM) images. It was found that at a Knudsen number of 1 COMET performs slower than the sequential procedure when no interfaces are involved. However, when interfaces are included in the domain, COMET outperforms the sequential procedure.

NOMENCLATURE

BZ	Brillouin zone
e''	non-equilibrium phonon energy density
$\Delta e''$	correction to e''
e^0	equilibrium phonon energy density
Δe^0	correction to e^0
f''	non-equilibrium phonon distribution function
$\hbar$	reduced Planck's constant
$\boldsymbol{K}$	phonon wave vector
Kn	Knudsen number
L	characteristic length
$\boldsymbol{n}$	normal vector
$\boldsymbol{q}$	heat flux vector
r	reflection coefficient
$\mathscr{R}$	reflection operator
t	transmission coefficient
$\mathscr{T}$	transmission operator
T	temperature
ΔT	correction to T
$\boldsymbol{v}$	phonon group velocity
v	magnitude of phonon group velocity
$\boldsymbol{x}$	position vector
$\Delta \boldsymbol{A}$	discrete area vector
$\Delta^3 \boldsymbol{K}$	wave vector control volume
ΔV	spatial control volume

Greek Letters

θ	dimensionless temperature
τ_{eff}	relaxation time
ω	phonon frequency

Subscripts
c pertaining to cell *c*
nb pertaining to neighbor cells
p polarization
ref reference value
0 pertaining to material 0
1 pertaining to material 1
01 implying a direction from 0 to 1
10 implying a direction from 1 to 0

BOLTZMANN TRANSPORT EQUATION

The steady Boltzmann transport equation (BTE) is a six-dimensional equation which tracks the probability density of phonon occupation. We solve the energy moment of the BTE, given by [27]:

$$\nabla\cdot\left(\boldsymbol{v}e''_p(\boldsymbol{x},\boldsymbol{K})\right)=\left(\frac{\partial e''_p(\boldsymbol{x},\boldsymbol{K})}{\partial t}\right)_{scattering} \qquad (1)$$
$$e''=\hbar\omega f''$$

The left hand side of Eq. (1) accounts for phonon free-flight, whereby a phonon travels uninterrupted with velocity $\boldsymbol{v}$, and energy density *e''*. The energy density is dependent on the wave vector $\boldsymbol{K}$, the polarization *p*, and the position vector $\boldsymbol{x}$. The phonon occupation number is *f*. The right hand side of Eq. (1) accounts for the loss or generation of phonon energy due to phonon-phonon scattering. In its full form, this term couples all phonons directly together, provided selection rules are satisfied [28]. Due to its complexity this term is often approximated through the use of a single mode relaxation time [20–22]:

$$\left(\frac{\partial e''_p(\boldsymbol{x},\boldsymbol{K})}{\partial t}\right)_{scattering}=\frac{e^0_p-e''_p}{\tau_{eff}}$$
$$e^0_p=\frac{\hbar\omega}{e^{\left(\frac{\hbar\omega}{k_BT}\right)}-1} \qquad (2)$$

This scattering kernel acts to drive the phonon energy density to an equilibrium energy density, e^0, which is the product of the phonon energy and the Bose-Einstein distribution function at a temperature *T*. The relaxation time, τ_{eff}, is the time-scale over which phonons of wave vector $\boldsymbol{K}$ relax to the Bose-Einstein distribution. It may be calculated from molecular dynamics [29], density functional theory with lattice dynamics [30–32], or curve fits to experimentally measured thermal conductivities [33].

Boundary Conditions

Two types of boundary conditions are considered here: given temperature and reflecting. At a given temperature boundary, it is assumed that phonons are brought to equilibrium at the boundary at a specified temperature T_{wall}. Therefore, any phonon being emitted from the boundary into the domain is assumed to be at the equilibrium energy density at the given wall temperature. Phonons leaving the domain are assumed to be perfectly absorbed into the boundary. Thus,

$$e''_{\boldsymbol{v}\cdot\boldsymbol{n}<0}(\boldsymbol{x}_b)=e^0(T_{wall}(\boldsymbol{x}_b))$$
$$e''_{\boldsymbol{v}\cdot\boldsymbol{n}>0}(\boldsymbol{x}_b)=e''_{\boldsymbol{v}\cdot\boldsymbol{n}>0}(\boldsymbol{x}_b^-) \qquad (3)$$

Here, $\boldsymbol{n}$ is the outward point normal, $\boldsymbol{x}_b$ is the position of the boundary, T_{wall} is the specified wall temperature, $\boldsymbol{x}_b^-$ is the position just inside the domain, next to the boundary.

At reflecting boundaries, a phonon may be specularly reflected, diffusely reflected, or reflected partly specularly and partly diffusely. When a phonon is specularly reflected, it undergoes a mirror reflection whereby its tangential velocity is the same but its normal velocity flips direction. When a phonon is diffusely reflected, it is assumed that the surface is rough enough to induce several scattering events which create a local equilibrium at the wall. All phonons are emitted at an equilibrium energy density which is the average of the phonon energy incident on the wall from inside the domain. The partially diffuse/partially specular wall boundary condition is shown below:

$$e''_{\boldsymbol{v}\cdot\boldsymbol{n}<0}(\boldsymbol{x}_b)=pe''(\boldsymbol{x}_b^-,\boldsymbol{K}_{spec})+(1-p)e^0(T_{diffuse})$$
$$\boldsymbol{K}_{spec}=\boldsymbol{K}-2(\boldsymbol{K}\cdot\boldsymbol{n})\boldsymbol{n}$$
$$e^0(T_{diffuse})=\frac{\hbar\omega}{exp\left(\frac{\hbar\omega}{k_BT_{diffuse}}\right)-1} \qquad (4)$$

Above, $\boldsymbol{K}_{spec}$ is wave vector which is a specular reflection of $\boldsymbol{K}$. The specularity parameter, *p*, is a number between 0 and 1. $T_{diffuse}$ is a temperature which satisfies the following relation:

$$\int_{\boldsymbol{v}\cdot\boldsymbol{n}<0}e^0(T_{diffuse})\boldsymbol{v}\cdot\boldsymbol{n}d^3\boldsymbol{K}=\int_{\boldsymbol{v}\cdot\boldsymbol{n}>0}e''\boldsymbol{v}\cdot\boldsymbol{n}d^3\boldsymbol{K} \qquad (5)$$

Interface Conditions

In this paper we assume that phonon scattering at the interface is elastic and that the surface is rough enough to cause diffuse reflection and transmission. Under these assumptions, a phonon transmitted across the interface transfers energy to phonon of any wave vector and polarization with the same frequency. In addition, the group velocity vector must point into the material into which the phonon is being transmitted. The same assumptions govern reflection as well. Using these stipulations, we seek to determine the transmission and reflection coefficients for both materials.

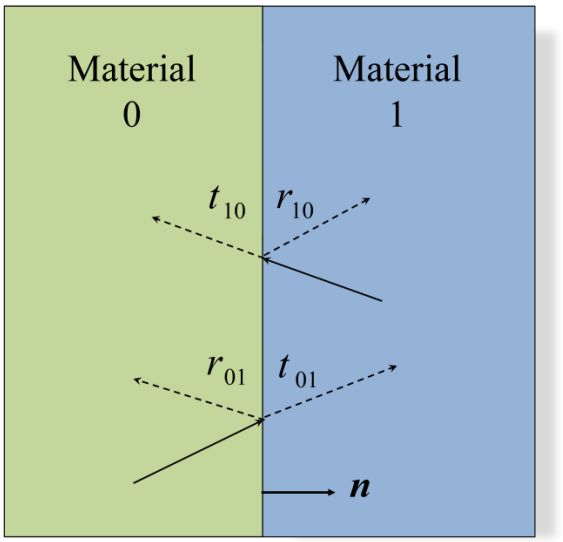

Figure 1: Simple schematic for an interface.

Following the convention in Fig. (1), we may write the following expressions for the transmissivity and reflectivity at the interface:

$$t_{01}(\omega)+r_{01}(\omega)=1 \tag{6}$$

$$t_{10}(\omega)+r_{10}(\omega)=1 \tag{7}$$

$$\left[\int_{\boldsymbol{v}\cdot\boldsymbol{n}>0} t_{01}(\omega)e^{0}(\omega,T)\boldsymbol{v}\cdot\boldsymbol{n}\delta(\omega)d^{3}\boldsymbol{K}\right]_{0} = -\left[\int_{\boldsymbol{v}\cdot\boldsymbol{n}<0} t_{10}(\omega)e^{0}(\omega,T)\boldsymbol{v}\cdot\boldsymbol{n}\delta(\omega)d^{3}\boldsymbol{K}\right]_{1} \tag{8}$$

Here, the subscript represents the direction of the incoming phonon. That is, t_{01} is the transmissivity of a phonon which is traveling from material 0 and being transmitted into material 1. Conversely, r_{10} is the reflectance of a phonon which is traveling in material 1 and being reflected off material 0. Equations (6) and (7) result from the conservation of energy at the interface resulting from elastic interactions. Equation (8) results from enforcing detailed balance for phonons of frequency ω; this is accounted for by the Dirac delta function, $\delta(\omega)$ in Eq. (8). Since there are four unknowns, we must find one more relationship in order to determine the transmissivity and reflectivity. The final relationship is obtained from a model for the transmission process. A number of models have been published in the literature, including the diffuse mismatch model (DMM) [34], transmission coefficients using the atomistic Green's function (AGF) approach [35,36], or those obtained from molecular dynamics (MD).

In this paper we will use the DMM as the fourth relation in determining the transmissivity and reflectivity:

$$t_{01}(\omega)=r_{10}(\omega);\ t_{10}(\omega)=r_{01}(\omega) \tag{9}$$

Using Eqs. (8) and (9), we may solve for the transmissivity:

$$t_{01}(\omega)=\frac{-\left[\int_{\boldsymbol{v}\cdot\boldsymbol{n}<0} e^{0}(\omega,T)\boldsymbol{v}\cdot\boldsymbol{n}\delta(\omega)d^{3}\boldsymbol{K}\right]_{1}}{\left[\int_{\boldsymbol{v}\cdot\boldsymbol{n}>0} e^{0}(\omega,T)\boldsymbol{v}\cdot\boldsymbol{n}\delta(\omega)d^{3}\boldsymbol{K}\right]_{0}-\left[\int_{\boldsymbol{v}\cdot\boldsymbol{n}<0} e^{0}(\omega,T)\boldsymbol{v}\cdot\boldsymbol{n}\delta(\omega)d^{3}\boldsymbol{K}\right]_{1}} \tag{10}$$

Using Eq. (10) it is possible to find the other three coefficients. In Eq. (10), the system is assumed to be in equilibrium which implies that the values of the equilibrium energy density at equal frequencies are the same, and may be cancelled out. However, as we will see later, due to the discrete nature of the problem at hand, we will be forced to allow dissimilar frequencies to interact.

NUMERICAL METHODS

The BTE is numerically solved using the COMET solution procedure, which is outlined in [23] and is briefly described here. The spatial and wave vector domain are discretized into arbitrary convex polyhedral cells which are shown in Figs. (2) and (3). Equation (1) is integrated over the cell to drive an energy balance for phonons of wave vector ***K***. The discretized counterpart to Eq. (1) is show in Eq. (11). Furthermore, an energy balance of the scattering kernel is also written in discrete form as Eq. (12).

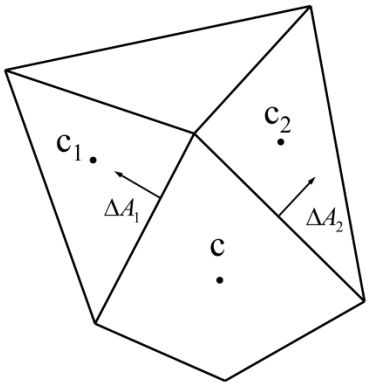

Figure 2: Spatial control volume.

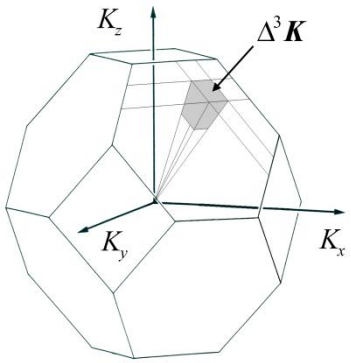

Figure 3: Wave vector control volume.

$$\sum_{\boldsymbol{v}\cdot\Delta\boldsymbol{A}_f>0}\Delta e_c''\boldsymbol{v}\cdot\Delta\boldsymbol{A}_f+\Delta e_c''\frac{\Delta V}{\tau_{eff}}-\Delta T_c\left(\frac{\partial e^0}{\partial T}\right)_{prev}\frac{\Delta V}{\tau_{eff}}=$$
$$-\left[\sum_{\boldsymbol{v}\cdot\Delta\boldsymbol{A}_f>0}e_c''\boldsymbol{v}\cdot\Delta\boldsymbol{A}_f+\sum_{\boldsymbol{v}\cdot\Delta\boldsymbol{A}_f<0}e_{nb}''\boldsymbol{v}\cdot\Delta\boldsymbol{A}_f-\frac{e_c^0-e_c''}{\tau_{eff}}\Delta V\right]_{prev}=-R \tag{11}$$

$$\Delta T_c\sum_{BZ}\left[\left(\frac{\partial e^0}{\partial T}\right)_{prev}\frac{\Delta^3\boldsymbol{K}}{\tau_{eff}}\right]-\sum_{BZ}\Delta e_c''\frac{\Delta^3\boldsymbol{K}}{\tau_{eff}}=$$
$$-\left[\sum_{BZ}\frac{e_c^0}{\tau_{eff}}\Delta^3\boldsymbol{K}-\sum_{BZ}\frac{e_c''}{\tau_{eff}}\Delta^3\boldsymbol{K}\right]_{prev}=-R_L \tag{12}$$

In Eq. (11), the summation on the left hand side is over all cell faces for which $\boldsymbol{v}\cdot\Delta\boldsymbol{A}_f>0$ where $\Delta\boldsymbol{A}_f$ is the outward-pointing area vector of face *f*. $\Delta e_c''$ and ΔT_c are corrections to the current solution at cell *c*. ΔV is the extent of the spatial control volume. *R* is the residual of Eq. (11) and includes the previous iterate (subscript "*prev*") values for the cell *c*, and its neighbor (subscript "*nb*") values. In Eq. (12), the summations are over the entire Brillouin zone (BZ) and all polarizations, and $\Delta^3\boldsymbol{K}$ is the extent of the wave vector control volume. R_L is the residual of Eq. (12).

Equations (11) and (12) form an "arrowhead" structured linear system which can be solved efficiently in *O(n)* operations, where *n* is the number of wave vector control volumes times the number of polarizations [23]. A flow chart of the solution procedure is shown in Fig. (4).

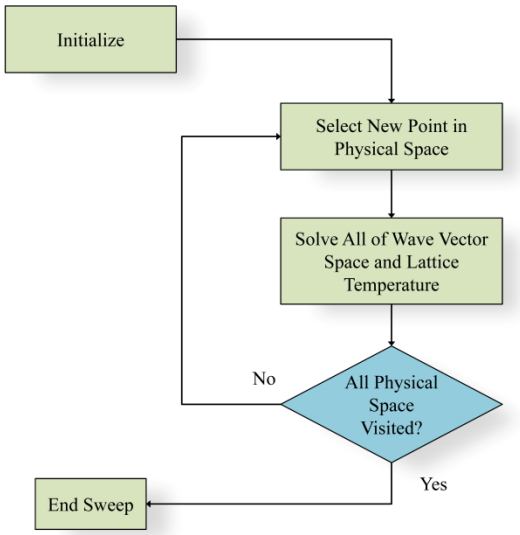

Figure 4: Flow chart for the COMET solution procedure.

After the solution has been initialized, one spatial cell is chosen. Within the spatial cell the arrowhead linear system is created for all wave vector space and solved directly. The next spatial cell is then chosen and a new linear system is created. This is repeated until all cells have been visited. To maintain spatial coupling, this smoothing procedure is embedded in a full approximation storage (FAS) geometric multigrid procedure [37]; the application to COMET is described in detail [23]

INTERFACE OPERATOR

Within the COMET framework, it is useful to think of the phonon energy at a spatial location as a vector quantity and the interface as an operator which projects the phonon energy onto either a different material represented by a different vector space, or the same material represented by the same vector space. All the details of the interface model are encapsulated in the structure of the interface operator. Using these interface operators, the interface condition may be written as:

$$\vec{E}_{i,1}''=\mathfrak{I}_{01}\vec{E}_0''+\mathfrak{R}_{10}\vec{E}_1''$$
$$\vec{E}_{i,0}''=\mathfrak{I}_{10}\vec{E}_1''+\mathfrak{R}_{01}\vec{E}_0'' \tag{13}$$

Here $\mathfrak{I}_{01}$ ($\mathfrak{I}_{10}$) is the transmission operator for phonons in material 0 (1) being transmitted to material 1 (0) and $\mathfrak{R}_{10}$ ($\mathfrak{R}_{01}$) is the reflection operator for phonons in material 1 (0) being reflected off an interface with material 0 (1). $\vec{E}_{i,1}''$ $\left(\vec{E}_{i,0}''\right)$ is the vector of phonon energy which is being emitted from the interface into material 1 (0).

To create the interface operator for the DMM, we first separate the wave vector space into frequency bins. By doing this, we effectively approximate the delta function in Eq. (10)

as a step function for the j^{th} frequency bin. It is equal to 1 when the frequency is between $\omega_{j,high}$ and $\omega_{j,low}$ and 0 everywhere else. Figure 5 shows the dispersion relation for silicon in the [100] direction with possible frequency bins marked as dotted lines. Possible wave vector control volume centroids are marked with black squares.

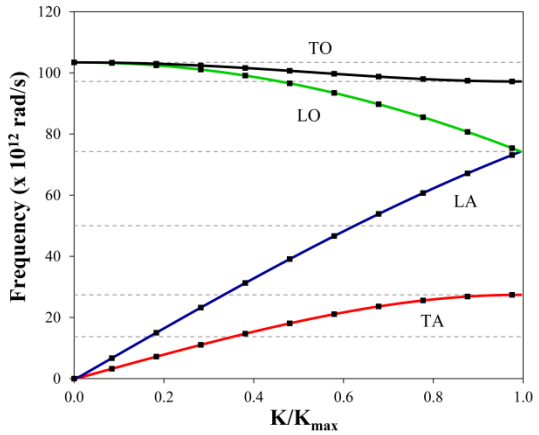

Figure 5: Dispersion relation for silicon in the [100] direction using the environment dependent interatomic potential (EDIP) [38]. The square symbols represent the discrete wave vectors $\boldsymbol{K}$ whose frequencies fall into the discrete frequency bins (shown by dotted lines).

If only small temperature differences occur in the problem, a constant specific heat may be assumed and the equilibrium energy density may then be written as:

$$e^0 \approx \left(\frac{\partial e^0}{\partial T}\right)_{ref}\left(T - T_{ref}\right) \tag{14}$$

We may insert Eq. (14) in Eq. (10) to obtain the transmission coefficient:

$$t_{01,j} = \frac{-\left[\sum_{i=1}^{N_{1,j}}\left(\frac{\partial e^0}{\partial T}\right)_{i,ref}\boldsymbol{v}_i\cdot\boldsymbol{n}\Delta^3\boldsymbol{K}_i\right]_1}{\left[\sum_{i=1}^{N_{0,j}}\left(\frac{\partial e^0}{\partial T}\right)_{i,ref}\boldsymbol{v}_i\cdot\boldsymbol{n}\Delta^3\boldsymbol{K}_i\right]_0 - \left[\sum_{i=1}^{N_{1,j}}\left(\frac{\partial e^0}{\partial T}\right)_{i,ref}\boldsymbol{v}_i\cdot\boldsymbol{n}\Delta^3\boldsymbol{K}_i\right]_1} \tag{15}$$

Above, the temperature dependence is cancelled out because it is assumed that a single interface temperature is used.

We now turn our attention to the creation of the transmission and reflection operators in Eq. (13). We start by calculating the heat flux $q''_{int,1,j}$ leaving the interface and entering material 1 in the j^{th} frequency band [25]:

$$q''_{int,1,j} = \left[t_{01,j}\sum_{i=1}^{N_{0,j}} e_i''\boldsymbol{v}_i\cdot\boldsymbol{n}\Delta^3\boldsymbol{K}_i\right]_0 - \left[r_{10,j}\sum_{i=1}^{N_{1,j}} e_i''\boldsymbol{v}_i\cdot\boldsymbol{n}\Delta^3\boldsymbol{K}_i\right]_1 \tag{16}$$

Knowing the heat flux for the j^{th} frequency bin, we determine the values for each e'' within the j^{th} in material 1 which have $\boldsymbol{v}\cdot\boldsymbol{n}>0$. Because there may be several different frequencies in the frequency bin, the heat flux must be distributed, so to speak, into each phonon such that the temperature is appropriate.
We distribute the phonon energy which is emitted from the interface in the j^{th} frequency bin into material 1 according to the following rule:

$$e_i'' = w_{i,1}q''_{int,1,j}$$

$$w_{i,1} = \left[\frac{\left(\frac{\partial e^0}{\partial T}\right)_{i,ref}}{\sum_{i=1}^{N'_{1,j}}\left(\frac{\partial e^0}{\partial T}\right)_{i,ref}\boldsymbol{v}\cdot\boldsymbol{n}\Delta^3\boldsymbol{K}_i}\right]_1 \tag{17}$$

which is the expression found in [25]. It should be noted that these weights will not add up to unity unless it is multiplied by $\boldsymbol{v}\cdot\boldsymbol{n}$ (and the wave vector volume). The summation of w by itself (with the wave vector volume) will give the inverse of the specific heat weighted average group velocity.

Using Eqs. (15), (16), and (17), the transmission operator from material 0 to 1 may be written as:

$$\left[\Im_{01}\right]_{i,k} = w_{i,1}t_{01}\boldsymbol{v}_k\cdot\boldsymbol{n}\Delta^3\boldsymbol{K}_k H\left(\boldsymbol{v}_k\cdot\boldsymbol{n}\right)H\left(\boldsymbol{v}_i\cdot\boldsymbol{n}\right) \tag{18}$$

In the equation above, i refers to the row index of the transmission operator which is also the index of the outgoing phonon in material 1. The i^{th} row of the transmission operator maps the i^{th} phonon to all the incoming phonons in the opposite material. The index k refers to the column of the transmission operator which is also the index of the phonon incident to the interface in material 0. The k^{th} column in the transmission operator will give a map of all phonons to which the k^{th} phonon in material 1 transmits energy to the phonons in material 0. The transmission coefficient t_{01} belongs to the frequency band to which the phonons i and k belong (if they are in different frequency bands the coefficient is zero). H is the Heaviside step function. A similar expression can be written for the reflection operator:

$$\left[\Re_{10}\right]_{i,k} = w_{i,1}r_{10}\boldsymbol{v}_k\cdot\boldsymbol{n}\Delta^3\boldsymbol{K}_k H\left(-\boldsymbol{v}_k\cdot\boldsymbol{n}\right)H\left(\boldsymbol{v}_i\cdot\boldsymbol{n}\right) \tag{19}$$

The i^{th} row of the reflection operator gives a list of all phonons which reflect energy into the i^{th} phonon. The k^{th} column gives a list of all phonons to which the k^{th} phonon reflects energy. All reflection operators are square matrices, whereas a transmission operator need not be. For each interface face, four interface operators must be created and stored.

Face Agglomeration

Crucial to the COMET solution procedure is the use of a FAS geometric multigrid. In order to accelerate convergence of the point-coupled procedure described above, a series of course meshes is created; solutions obtained on these coarse meshes provide corrections to finer mesh levels to accelerate convergence [37].

Coarse level meshes are created by agglomerating fine level cells together. During mesh creation, for computational efficiency, when two fine-level cells are agglomerated, new coarse faces are created by summing fine level faces which have common coarse cells.

Because of the Heaviside step functions in Eqs. (18) and (19), the number of non-zero elements in both operators is ~25%. For a practical problem, the number of discrete phonons can range from a few hundreds to a few thousand. Since we must create four interface operators per interface face, there is computational gain in minimizing the number of interface faces at all mesh levels. Furthermore, an effective transmission/reflection operator must be defined at all multigrid mesh levels. In this paper, the equivalent interface operator (for both reflection and transmission) is written as:

$$\Im_{I,01} = \sum_{i \in I} \frac{\Delta \boldsymbol{A}_I \cdot \Delta \boldsymbol{A}_i}{\Delta \boldsymbol{A}_I \cdot \Delta \boldsymbol{A}_I} \Im_{i,01}$$
$$\Delta \boldsymbol{A}_I = \sum_{i \in I} \Delta \boldsymbol{A}_i \qquad (20)$$

Here, the summations are over all finer level faces, i, which make up the coarse level face, I.

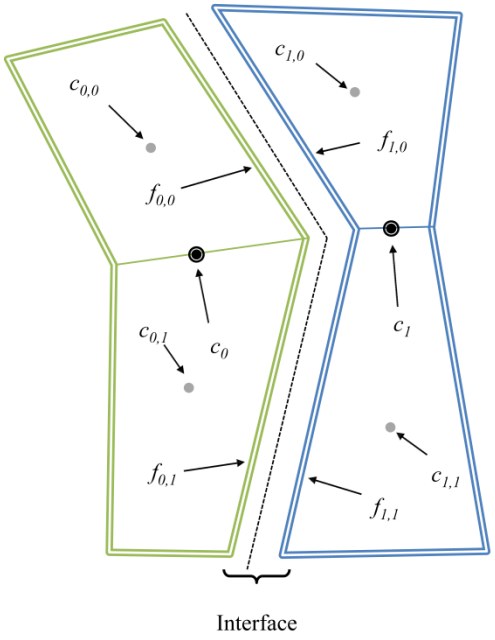

Figure 6: Schematic of the interface face agglomeration.

For example, using Fig. (6), let us say that cell $c_{0,0}$ and cell $c_{0,1}$ combine to make a coarse level cell c_0. Correspondingly, cell $c_{1,1}$ and cell $c_{1,1}$ combine to make a coarse cell c_1. We can then combine faces $f_{0,1}$ and $f_{0,0}$ to make a coarse level face and combine faces $f_{1,0}$ and $f_{1,1}$ to make a coarse level face. When coming up with the transmission or reflection operator for cell c_0, the summation will be over faces $f_{0,0}$ and $f_{0,1}$. When finding the transmission or reflection operator for c_1, the summations will be over face $f_{1,0}$ and $f_{1,1}$.

Partially Implicit Treatment

For a given cell which is on an interface, Eq. (13) has a phonon energy contribution from the neighboring cell on the other side of the interface, and a component from the current cell of interest. Because of this dependence, the solution at any interface cell may be treated in a partially implicit manner. This treatment is similar to the way boundary conditions are handled in [23]. After one iteration of the point linear system, Eq. (13) is updated using the latest values of the solution vector. This gives us new values for the interface. This procedure adds non-linearity to the point coupled solution, but was seen to increase convergence rates.

RESULTS

In this section, we test the performance of the COMET procedure for interface transport by comparing it with the performance of a conventional sequential solution procedure for a variety of test problems.

One-Dimensional Phonon Transport in a Composite

To get an accurate comparison between the two methods, we first consider only ballistic transport in gray mediums. Choosing the ballistic limit eliminates COMET acceleration obtained due to more efficient treatment of bulk scattering, as described in [23]. Thus, solution acceleration due only to the interface treatment may be gauged. We consider a one-dimensional domain, as shown in Fig. (6), and vary the number of interfaces. The total number of cells in all three domains is set to 640. In keeping with a gray approximation, a spherical Brillouin zone is employed and discretized using spherical coordinates [39]. In the angular space, a discretization of N_θxN_ϕ=4x4 in the octant is used; here θ is the polar angle and ϕ is the azimuthal angle, as described in [23]. In these problems, only one multigrid level was needed to reach convergence in one iteration, or adding levels beyond 2 caused a slower time to convergence. Therefore we report timing for 1 level, but also show iteration count and total solution time for different multigrid levels. A standard V-cycle was used for all results [37].

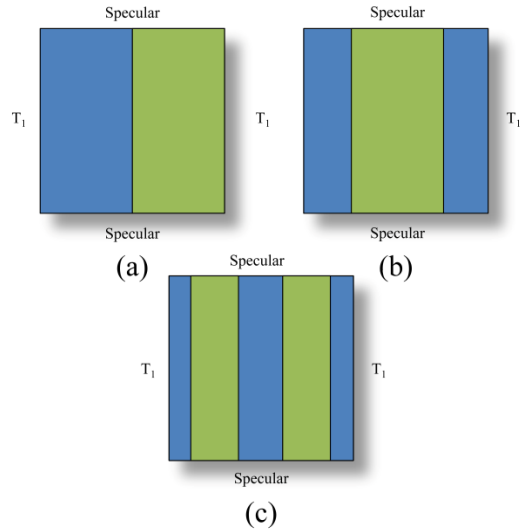

Figure 7: Different one dimensional domains used for comparison. The total number of cells for all three domains is 640.

For all the simulations in this paper, we assume a constant specific heat. The solution is initialized to T_i=301 K. The boundary conditions on the left and right are set at T_1=300 K. The solution is considered converged when the dimensionless temperature, defined as

$$\theta = \frac{T - T_1}{T_i - T_1} \tag{21}$$

falls below 10^{-6}. This criteria was used for both COMET and the sequential procedure.

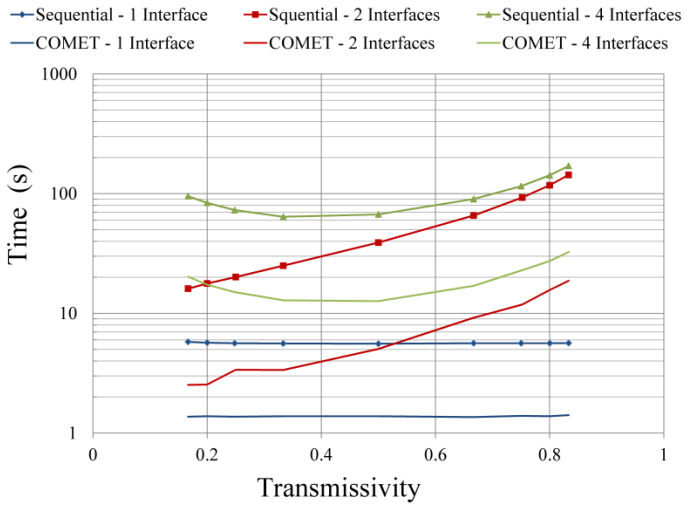

Figure 8: Total solution time for COMET and the sequential procedure for the domains pictured in Fig. (7).

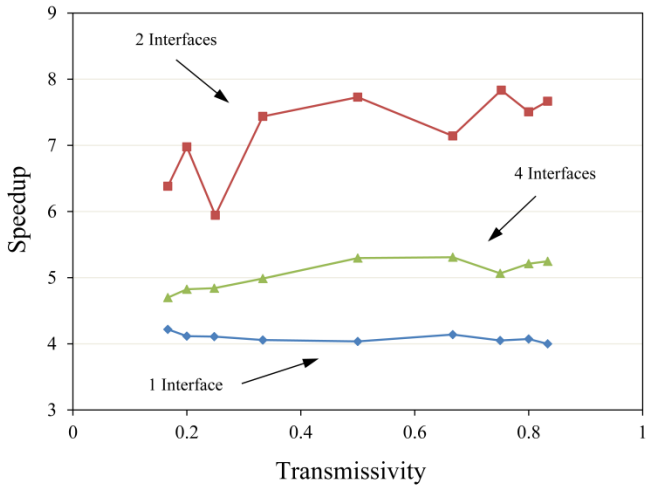

Figure 9: CPU Speedup of COMET over the sequential procedure attained for the domains shown in Fig. (7).

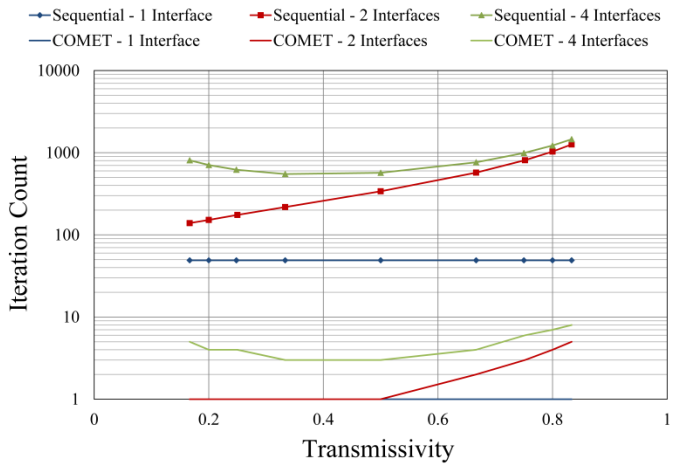

Figure 10: Iteration count for COMET and the sequential procedure as a function of transmissivity for the different domains pictured in Fig. (7).

Figures (8)-(10) summarize the results by showing the total solution time for COMET and the sequential procedure, the speedup in total solution time of COMET compared to the sequential procedure, and the iteration count for COMET and the sequential procedure, respectively, as a function of transmissivity for different number of interfaces. By eliminating spatial coupling, we can see that indeed, because of the implicit treatment at the interfaces, the COMET procedure outperforms the sequential procedure for all cases, delivering an acceleration factor in CPU time of 4-8. When only one interface is in the domain (Fig (7a)), the sequential procedure performance is not hindered to a large degree. This is why we see the lowest speedup here. Adding a second interface hinders the sequential procedure more so because the middle material is completely isolated from a boundary. At four interfaces, the

speedup drops to ~5, however. The reason pertains to the cost of computing the interface values. It was found that for Figs. (7b) and (7c), adding multigrid levels decreased the iteration count, but did not reduce the total compute time. Because this is a 1-dimensional domain, each interface represents 1 face. With this setup, it is not possible to reduce the number of interface faces for subsequent coarse levels, which leads to a higher cost per coarse level. A plot of the total solution time as a function of transmissivity for different multigrid levels is shown in Fig. (11). For one interface, the solution time increases because only one iteration is needed for the solution to converge with one level.

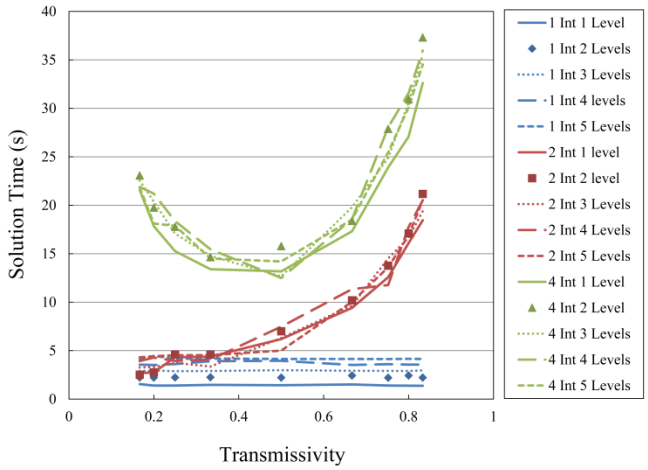

Figure 11: Total solution time taken for COMET as a function of transmissivity for varying domains pictured in Fig. (7) and different multigrid levels.

It should be noted that the domains pictured Fig. (7) represent the worst case scenario for convergence. This is because all phonons must be transmitted across the interface, and there are no pathways between the boundaries that do not encounter the interface. Thus the bottlenecks to convergence because of the interface treatment are the worst for this problem.

Heat Conduction in Two-Dimensional Particle Bed

Next, we consider phonon transport in a two-dimensional particle composite, as shown in Fig. (12).

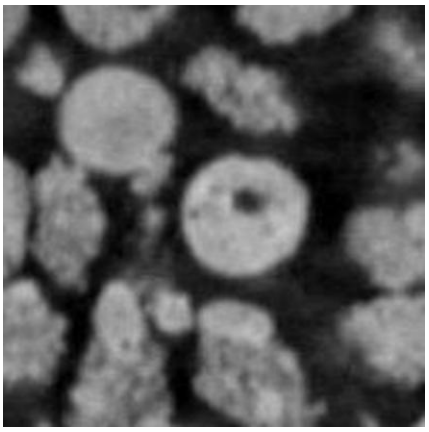

Figure 12: X-ray CT Scanned image of nanoparticle composite.

The composite consists of silicon particles embedded in a matrix of germanium. The diameter of the particles in the composite is approximately 250 micrometers. The volume fraction of the particles (ratio of total particle volume to total volume) is approximately 31%.

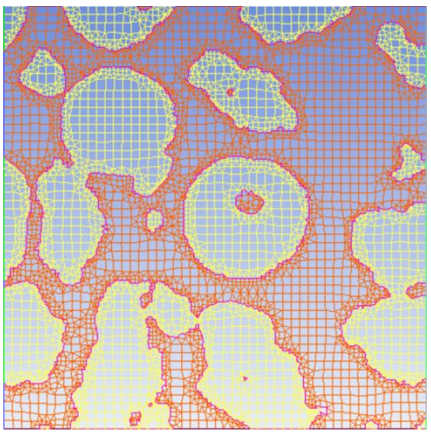

Figure 13: Mesh generated for image shown in Fig. (12).

The geometry of the particle composite is obtained as a 2D image using x-ray micro-CT scanning. Figure (12) shows a representative scan. The differential absorptivity of x-rays by different materials leads to difference in the grayscale intensities of the scanned image. The first step is to partition the image into different sub regions so that respective properties of the constituent materials can be assigned. This process is called segmentation and is carried out using the open source software package OOF2 [40]. OOF2 also has image processing capabilities like noise removal, thresholding, and downsampling that are used to process the image. Once the image is segmented, OOF2 can generate finite volume meshes. Figure (13) shows the finite volume mesh for the image shown in Fig. (12). The actual size of the image taken is 400x400 μm, but the domain is scaled to obtain the desired Knudsen number. The mesh contains 8,194 finite volume cells; a mixture of quadrilaterals and triangles is used.

We will first benchmark against the sequential procedure using a gray dispersion relation. A T_1=300 K boundary condition on all walls will be used with an initial guess of T_i=301 K. The convergence criteria described in Eq. (21) will also be used for both COMET and the sequential procedure. After the method is benchmarked against the sequential procedure, we will examine the particle composite using realistic dispersions for silicon and germanium.

Influence of Interface Agglomeration

Strategies for agglomeration of interface faces play a critical role in convergence acceleration. As mentioned earlier, in creating coarse levels in the geometric multigrid procedure, in addition to agglomerating fine-level cells, fine-level interfaces in the mesh must be agglomerated as well, and the corresponding effective interface transmission operators created at each mesh level. To demonstrate the importance of this effective operator, we first consider a scenario in which, at each coarse level, no care is taken to preferentially agglomerate interface cells together. With this strategy, minimal interface agglomeration occurs at each coarse level, so that the number of interfaces at coarse levels does not decreases by the factor of two enforced on the volumetric cells. Thus, the coarse-level interface faces impose a penalty on solution time which may overshadow the overall decrease in iteration count that the multigrid procedure can deliver.

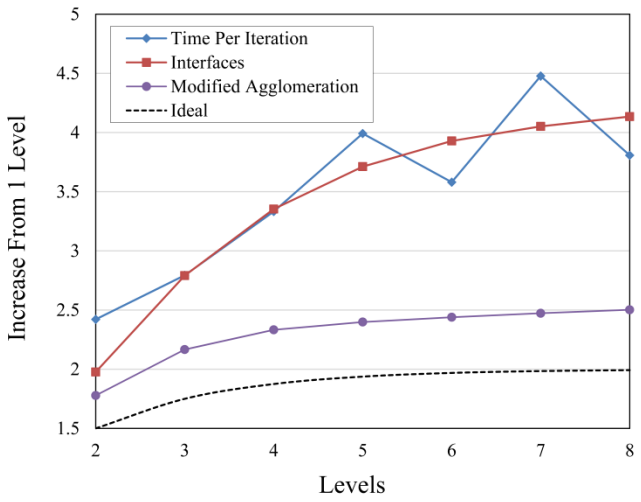

Figure 14: Increase in the time taken per COMET iteration and the increase in the number of total interfaces.

Figure (14) shows the increase in time per COMET iteration for each additional coarse level relative to a single fine level iteration. In the ideal scenario, the additional effort for each additional multigrid level should follow closely to the dashed line in Fig. (14). This line was found by assuming that an additional level carries an additional cost which is half that of the previous level. The red curve in Fig. (14) shows the additional number of *total* interface faces in the simulation (summation over all levels). The solid blue curve is the time per iteration of COMET. We can see that the solid blue and red curves follow one another closely; COMET cost is dominated in this problem by the cost of interface computation, and thus scales approximately as the total number of interfaces summed over all mesh levels. Significant computational gains may be had by reducing the number of interface faces at the coarse mesh levels.

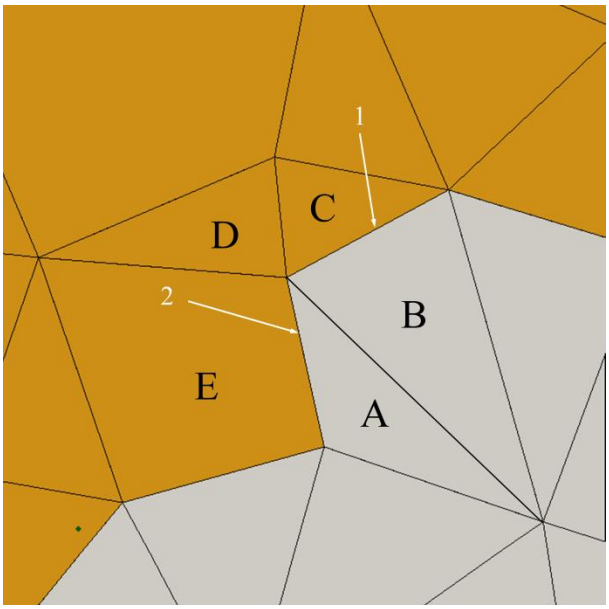

Figure 15: Close up of the mesh shown in Fig. (9) at an interface.

It was found that a successful agglomeration strategy must aggressively target interface faces to agglomerate before any interior cell agglomeration occurred. Of particular importance is the scenario pictured in Fig. (15). Here, the two different materials are shown, one in orange and one in gray. If cells A and B were chosen to be agglomerated together, in order to agglomerate faces 1 and 2 cells C, D, and E would need to have also been selected for agglomeration. This cannot be left to chance, so a successful agglomeration strategy must also find "bridge" cells (cell D in this case) which would allow more interface agglomeration. We have explored heuristically a number of interface agglomeration strategies. One such strategy, which achieves face agglomeration by an approximate factor of two, is explored in Fig. (14). We see that the ideal number of total interface faces must saturate at two as the number of coarse levels increases (black dashed line). The modified agglomeration strategy (violet circles) does not quite achieve this ideal limit, but is substantially more effective than a random agglomeration strategy.

Comparison of COMET with Sequential Procedure

For comparison with the sequential procedure we will again use a gray BTE and vary the transmissivity. However, here we will use two different, moderate Knudsen numbers to include the effect of volumetric scattering. We consider a particle mesh

similar to that in Fig. (13), with 8,194 cells, and 1412 interface faces. The dimensionless parameters governing the problem are the domain Knudsen number, which is the mean free path divided by the domain length, the particle Knudsen number which is the mean free path divided by the largest particle size ($Kn_p \sim 3.4Kn$), and the interface transmissivity. We consider two domain Knudsen numbers, Kn = 1 and 10. The interface transmissivity is varied and the performance of COMET is compared with that of the sequential procedure.

The results of the comparison are summarized in Fig. (16). The dashed lines denote the acceleration obtained by COMET over the sequential procedure for a domain with no interfaces, but the same domain Knudsen number. We see that in the absence of interfaces, COMET outperforms the sequential solver for the lower Knudsen number (Kn=0.1), but incurs a performance penalty for Kn = 1.0, as discussed in [23]. Here we seek to compare COMET performance with that of the sequential procedure in the presence of complex interfaces as in the particle composite in Fig. (13).

For the lower Knudsen number, Kn=0.1, we see that acceleration in CPU time is obtained using the COMET procedure for all transmissivities considered. COMET acceleration factors exceed those for the case with no interfaces. This is because interface coupling of phonons in ***K*** space is more effectively handled by the point-coupled nature of COMET. However, the acceleration factor obtained in the presence of interfaces depends on the interface transmissivity. For the higher Knudsen number, Kn=1.0, CPU time acceleration is not obtained for all transmissivities, but even so, better performance than the no-interface case is obtained in all cases.

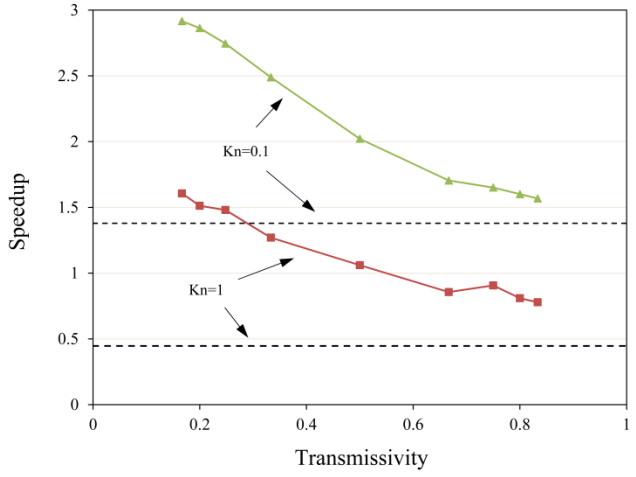

Figure 16: Speedup in CPU time attained for varying transmissivity and Knudsen number. Dashed lines represent speedup attained when no interface is present.

***K**-resolved Phonon Transport in 2D Particle Composite*

Finally, we consider phonon transport in the domain pictured in Fig. (13) using realistic dispersion relations for silicon and germanium. The simulation is performed only using COMET; the sequential procedure has great difficulty converging in this case and is not pursued. The particles are made of silicon and the matrix of germanium. The dispersion relation for silicon and germanium, shown below, is found using the environment dependent interatomic potential [38] and the Harrison potential [41], respectively.

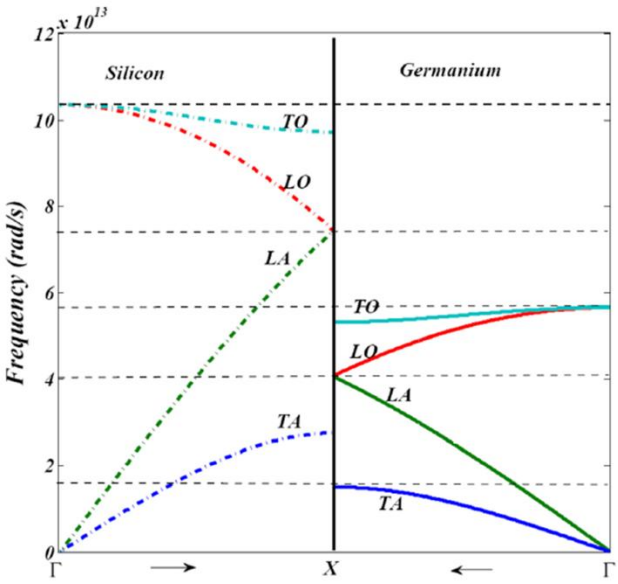

Figure 17: Dispersion relation for silicon [38] and germanium [41]. Figure adapted from [25].

The relaxation time is found using the procedures outlined in [42]:

$$\tau_{im}^{-1} = A\omega^4$$
$$\tau_u^{-1} = BT\omega^2 e^{-C/T} \qquad (22)$$

τ_{im} is the relaxation time for impurity scattering and τ_u is the relaxation time for Umklapp scattering. The parameters in Eq. (22) are found by fitting bulk thermal conductivity to experimental data in [33]. It is found that for Si, A=1.32x10^{-45} s^3, B=1.73x10^{-19} s/K, and C=137.39 K. The parameters for Ge are A=2.4x10^{-44} s^3, B=3.35x10^{-19} s/K, and C=57.6 K. The scattering rates are combined using Mattheissen's rule to create an effective scattering rate:

$$\tau_{eff}^{-1} = \tau_{im}^{-1} + \tau_u^{-1} \qquad (23)$$

The domain length is 316.5 nm which leads to an average bulk Knudsen number of 0.186 in silicon and 0.123 in germanium. The boundary conditions on the top and bottom walls are set to be specularly reflecting while the boundary conditions on the right and left walls are set to T_1=300 K and T_2=301 K, respectively. For both silicon and germanium, an isotropic Brillouin zone is assumed with an angular discretization of N_θxN_ϕ=2x2 in the octant. The wave vector magnitude is

discretized into 10 equal length segments. Frequencies are binned into five different frequency bins at the interface. The first four bins are equally spaced between 0 and the maximum frequency in germanium, ω=5.65 x 10^{13} rad/s. The fifth bin stretches from the maximum frequency in germanium to the maximum frequency in silicon, ω=1.03 x 10^{14}.

Figure (18) shows a contour plot of the dimensionless lattice temperature, $T^*=(T-T_1)/(T_2-T_1)$. We can see there are finite temperature drops at interfaces as well as steep drops in temperature where silicon particles are in close proximity to each other, which constricts heat flow in germanium.

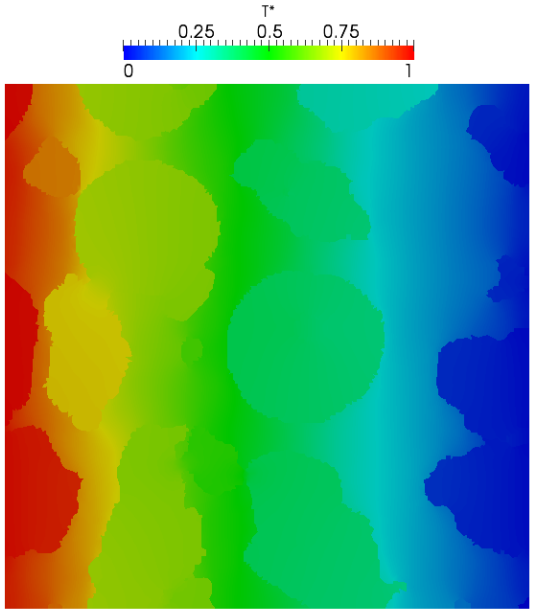

Figure 18: Contour plot of the lattice temperature (K).

Figure (19) shows a plot of the lattice temperature as well as the temperature of the different braches along the dimensionless x^* at y^*=0.5. Branch temperatures are calculated by finding the total energy of all phonons in the given branch, and solving for the equilibrium temperature which corresponds to that same energy. In this case it is a linear solve, due to the constant specific heat assumption. Here we can clearly see the aforementioned temperature drops at the interfaces. Both particles show signs of non-equilibrium behavior, particularly in the largest particle which has an average Knudsen number (in silicon) of Kn_p=0.63 and a maximum Knudsen number $Kn_{p,max}$=255.

Lastly, we show a contour plot of the dimensionless total heat flux in the x-direction in Fig. (20). The values are non-dimensionalized by the heat flux obtained under the same temperature difference and domain length for a sample of pure germanium. The largest value occurs when three silicon particles meet, and form a constrictive pathway for the heat to flow. An interesting note is that the majority of the low values occur in regions where the interface is parallel to the direction of heat flow, with the lowest values being ~<10% of the interface-free heat flux. Areas where there is a clear path from one boundary to the other show roughly 80% of the interface free value.

The effective thermal conductivity of the domain shown is 12.39 W/m^{2}K. For pure germanium and silicon, the conductivity is 23.64 W/m^{2}K and 58.61 W/m^{2}K, respectively. Despite adding a more conductive material to germanium, interface resistances have reduced the conductivity by a value of nearly 50%.

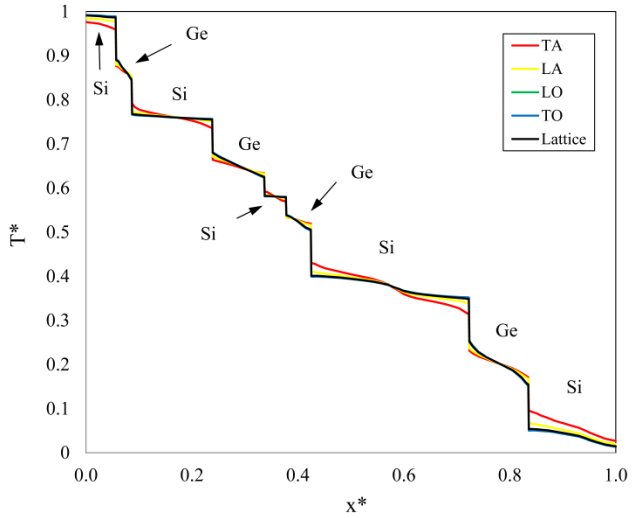

Figure 19: Dimensionless temperature of the lattice and phonon branches for the horizontal line at y^*=0.5.

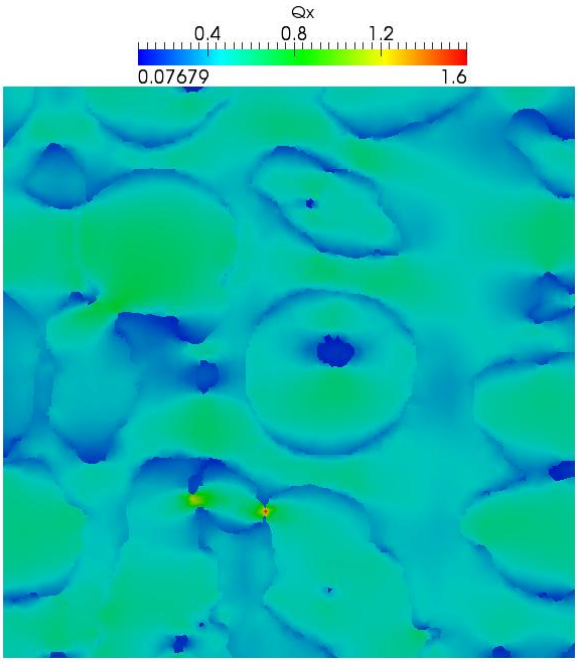

Figure 20: Contour plot of the dimensionless x-direction heat flux.

CONCLUSIONS

In this paper, we have extended the coupled ordinates method (COMET) for the solution of the phonon Boltzmann transport equation to include phonon transport at interfaces. A general transmission/reflection operator was developed which could be tailored for a wide range of transmission models. The method was benchmarked against the conventional sequential solution procedure and shown to have better convergence rates for problems with interfaces. Furthermore, we have demonstrated power of the solution procedure by simulating, for the first time, phonon transport in a nanoparticle composite using a ***K***-resolved Brillouin zone. The COMET procedure has thus been shown to be a viable computational method for a range of complex phonon transport problems.

ACKNOWLEDGMENTS

The authors would like to thank Dr. Dhruv Singh for useful discussions and providing the dispersion relations for germanium and silicon.

REFERENCES

[1] Poudel B., Hao Q., Ma Y., Lan Y., Minnich A., Yu B., Yan X., Wang D., Muto A., Vashaee D., Chen X., Liu J., Dresselhaus M. S., Chen G., and Ren Z., 2008, "High-Thermoelectric Performance of Nanostructured Bismuth Antimony Telluride Bulk Alloys," Science, **320**(5876), pp. 634–8.

[2] Yu B., Zebarjadi M., Wang H., Lukas K., Wang H., Wang D., Opeil C., Dresselhaus M., Chen G., and Ren Z., 2012, "Enhancement of Thermoelectric Properties by Modulation-Doping in Silicon Germanium Alloy Nanocomposites.," Nano letters, pp. 6–11.

[3] Hao Q., Zhu G., Joshi G., Wang X., Minnich A., Ren Z., and Chen G., 2010, "Theoretical Studies on the Thermoelectric Figure of Merit of Nanograined Bulk Silicon," Applied Physics Letters, **97**(6), p. 063109.

[4] Zide J. M. O., Bahk J.-H., Singh R., Zebarjadi M., Zeng G., Lu H., Feser J. P., Xu D., Singer S. L., Bian Z. X., Majumdar A., Bowers J. E., Shakouri A., and Gossard a. C., 2010, "High Efficiency Semimetal/Semiconductor Nanocomposite Thermoelectric Materials," Journal of Applied Physics, **108**(12), p. 123702.

[5] Zebarjadi M., Joshi G., Zhu G., Yu B., Minnich A., Lan Y., Wang X., Dresselhaus M., Ren Z., and Chen G., 2011, "Power Factor Enhancement by Modulation Doping in Bulk Nanocomposites," Nano Letters, **11**, pp. 2225–2230.

[6] Kim W., Zide J., Gossard A., Klenov D., Stemmer S., Shakouri A., and Majumdar A., 2006, "Thermal Conductivity Reduction and Thermoelectric Figure of Merit Increase by Embedding Nanoparticles in Crystalline Semiconductors," Physical Review Letters, **96**(4), p. 045901.

[7] Lee J.-H., Galli G. A., and Grossman J. C., 2008, "Nanoporous Si as an Efficient Thermoelectric Material," Nano letters, **8**(11), pp. 3750–4.

[8] Mingo N., Hauser D., Kobayashi N. P., Plissonnier M., and Shakouri A., 2009, "' Nanoparticle-in-Alloy ' Approach to Efficient Thermoelectrics : Silicides in SiGe," Nano Letters, **9**(2), pp. 711–715.

[9] Lundstrom M., 2000, Fundamentals of Carrier Transport, Cambridge University Press, New York, NY.

[10] Mahan G., Sales B., and Sharp J., 1997, "Thermoelectric Materials: New Approaches to an Old Problem," Physics Today, **50**(3), pp. 42–47.

[11] Venkatasubramanian R., Siivola E., Colpitts T., and O'Quinn B., 2001, "Thin-film Thermoelectric Devices with High Room-Temperature Figures of Merit," Nature, **413**(6856), pp. 597–602.

[12] Harman T. C., Harman T. C., Taylor P. J., Walsh M. P., and Laforge B. E., 2002, "Quantum Dot Superlattice Thermoelectric Materials and Devices," Science, **297**, pp. 2229–2232.

[13] Hsu K. F., Loo S., Guo F., Chen W., Dyck J. S., Uher C., Hogan T., Polychroniadis E. K., and Kanatzidis M. G., 2004, "Cubic AgPb(m) SbTe(2+m) : Bulk Thermoelectric Materials with High Figure of Merit," Science, **303**, pp. 818–821.

[14] Mazumder S., and Majumdar A., 2001, "Monte Carlo Study of Phonon Transport in Solid Thin Films Including Dispersion and Polarization," ASME Journal of Heat Transfer, **123**(4), p. 749.

[15] Mittal A., and Mazumder S., 2010, "Monte Carlo Study of Phonon Heat Conduction in Silicon Thin Films Including Contributions of Optical Phonons," ASME Journal of Heat Transfer, **132**, p. 052402.

[16] Péraud J.-P. M., and Hadjiconstantinou N. G., 2011, "Efficient Simulation of Multidimensional Phonon Transport Using Energy-Based Variance-Reduced

Monte Carlo Formulations," Physical Review B, **84**(20), p. 205331.

[17] Péraud J.-P. M., and Hadjiconstantinou N. G., 2012, "An alternative Approach to Efficient Simulation of Micro/Nanoscale Phonon Transport," Applied Physics Letters, **101**(15), p. 153114.

[18] Jeng M.-S., Yang R., Song D., and Chen G., 2008, "Modeling the Thermal Conductivity and Phonon Transport in Nanoparticle Composites Using Monte Carlo Simulation," Journal of Heat Transfer, **130**(4), p. 042410.

[19] Tian W., and Yang R., 2007, "Effect of Interface Scattering on Phonon Thermal Conductivity Percolation in Random Nanowire Composites," Applied Physics Letters, **90**(26), p. 263105.

[20] Narumanchi S. V. J., Murthy J. Y., and Amon C. H., 2004, "Submicron Heat Transport Model in Silicon Accounting for Phonon Dispersion and Polarization," ASME Journal of Heat Transfer, **126**(6), p. 946.

[21] Narumanchi S. V. J., Murthy J. Y., and Amon C. H., 2005, "Comparison of Different Phonon Transport Models for Predicting Heat Conduction in Silicon-on-Insulator Transistors," Journal of Heat Transfer, **127**(7), p. 713.

[22] Narumanchi S. V. J., Murthy J. Y., and Amon C. H., 2005, "Boltzmann Transport Equation-Based Thermal Modeling Approaches for Hotspots in Microelectronics," Heat and Mass Transfer, **42**(6), pp. 478–491.

[23] Loy J. M., Mathur S. R., and Murthy J. Y., 2013, "A Coupled Ordinates Method for the Convergence Acceleration of the Phonon Boltzmann Transport Equation," ASME Journal of Heat Transfer, (Submitted).

[24] Little W. A., 1959, "The Transport of Heat Between Dissimilar Solids at Low Temperatures," Canadian Journal of Physics, **37**(3), pp. 334–349.

[25] Singh D., Murthy J. Y., and Fisher T. S., 2011, "Effect of Phonon Dispersion on Thermal Conduction Across Si/Ge Interfaces," ASME Journal of Heat Transfer, **133**(12), p. 122401.

[26] Huang Z., Singh D., Murthy J. Y., and Fisher T. S., 2009, "Boltzmann Transport Equation Simulation of Semiconductor Interfacial Heat Transfer Based on Input from the Atomistic Green's Function Method," Materials Research Society Symposia Proceedings, **1172**(Symposium T).

[27] Kittel C., 1996, Introduction to Solid State Physics, Wiley, New York, NY.

[28] Ziman J. M., 1963, Electrons and Phonons, Oxford University Press, Oxford.

[29] Henry A. S., and Chen G., 2008, "Spectral Phonon Transport Properties of Silicon Based on Molecular Dynamics Simulations and Lattice Dynamics," Journal of Computational and Theoretical Nanoscience, **5**(2), pp. 1–12.

[30] Ward A., and Broido D. A., 2010, "Intrinsic Phonon Relaxation Times from First-Principles Studies of the Thermal Conductivities of Si and Ge," Physical Review B, **81**(8), pp. 1–5.

[31] Broido D. A., Malorny M., Birner G., Mingo N., and Stewart D. A., 2007, "Intrinsic Lattice Thermal Conductivity of Semiconductors from First Principles," Applied Physics Letters, **91**(23), p. 231922.

[32] Ward A., Broido D., Stewart D., and Deinzer G., 2009, "Ab Initio Theory of the Lattice Thermal Conductivity in Diamond," Physical Review B, **80**(12), pp. 1–8.

[33] Glassbrenner C. J., and Slack G. A., 1966, "Thermal Conductivity of Silicon and Germanium from 3 K to the Melting Point," Physical Review, **134**(4A), pp. A1058–A1069.

[34] Swartz E. T., and Pohl R. O., 1987, "Thermal Resistance at Interfaces," Applied Physics Letters, **51**(26), pp. 2200–2202.

[35] Zhang W., Fisher T. S., and Mingo N., 2007, "The Atomistic Green's Function Method: An Efficient Simulation Approach for Nanoscale Phonon Transport," Numerical Heat Transfer, Part B: Fundamentals, **51**, pp. 333–349.

[36] Tian Z., Esfarjani K., and Chen G., 2012, "Enhancing Phonon Transmission Across a Si/Ge Interface by Atomic Roughness: First-Principles Study with the Green's Function Method," Physical Review B, **86**(23), p. 235304.

[37] Brandt A., and Livne O. E., 2011, Multigrid Techniques, SIAM, Philadelphia, PA.

[38] Bazant M. Z., Kaxiras E., and Justo J. F., 1997, "Environment-Dependent Interatomic Potential for Bulk Silicon," Physical Review B, **56**(14), pp. 8542–8552.

[39] Chai J. C., Lee H. S., and Patankar S. V., 1994, "Finite Volume Method for Radiation Heat Transfer," Journal of Thermophysics and Heat Transfer, **8**(3), pp. 419–425.

[40] "http://www.ctcms.nist.gov/oof/oof2/."

[41] Harrison W. A., 9189, Electronic Structure and the Properties of Solids, Dover, Mineola, NY.

[42] Mingo N., Yang L., Li D., and Majumdar A., 2003, "Predicting the Thermal Conductivity of Si and Ge Nanowires," Nano Letters, **3**(12), pp. 1713–1716.